frontiers | Frontiers in Energy Research

TYPE Original Research
PUBLISHED 18 October 2024
DOI 10.3389/fenrg.2024.1473060

OPEN ACCESS

EDITED BY
Roberto Francisco Coelho,
Federal University of Santa Catarina, Brazil

REVIEWED BY
Shiqi Jiang,
Harbin Institute of Technology, China
Thiago Fonseca Rech,
Federal University of Santa Catarina, Brazil

*CORRESPONDENCE
Wenyong Guo,
✉ wyguo@bjtu.edu.cn
Gang Xu,
✉ aaronxug@126.com
Tongzhen Wei,
✉ tzwei@mail.iee.ac.cn

RECEIVED 30 July 2024
ACCEPTED 18 September 2024
PUBLISHED 18 October 2024

CITATION
Sang W, Guo W, Xu G, Wei T, Shi C, Liu Z, Xue H, He Z, Li J, Shen J, Min R, Song S, Li X and Hong Y (2024) A novel robust active damping control strategy based on H∞ loop shaping for the grid-tied LCL inverter.
Front. Energy Res. 12:1473060.
doi: 10.3389/fenrg.2024.1473060

A novel robust active damping control strategy based on H∞ loop shaping for the grid-tied LCL inverter

Wenju Sang[1,2], Wenyong Guo[3]*, Gang Xu[4]*, Tongzhen Wei[1,2]*, Changli Shi[1,2], Zongjie Liu[5], Han Xue[5], Zhenning He[4], Junzhi Li[6], Jiazhen Shen[3], Ruiqi Min[3], Shaobo Song[3], Xiaoxu Li[3] and Yun Hong[3]

[1]Institute of Electrical Engineering, Chinese Academy of Sciences, Beijing, China, [2]University of Chinese Academy of Sciences, Beijing, China, [3]School of Electrical Engineering, Bejing Jiaotong University, Beijing, China, [4]Shanghai Institute of Satellite Engineering, Shanghai, China, [5]State Grid Shandong Electric Power Company, Jinan, China, [6]R&D Department at Hiconics Eco-energy Technology Co., Ltd., Beijing, China

LCL-type grid-connected inverters have been widely used in renewable power generation due to their size and cost advantages. However, the LCL filter has a problem of insufficient damping, which may lead to power system instability. Two common methods are used to address this problem: passive damping (PD) and active damping (AD). PD methods suppress resonance by adding resistors to the LCL filter, but this approach increases system losses. AD methods enhance damping through control to suppress resonance. Existing AD methods are often significantly affected by grid-side inductance perturbation, resulting in insufficient robustness. To address this issue, this article proposes a novel robust active damping (RAD) control strategy based on H∞ loop shaping. Simulation analysis and experimental research show that the RAD control method exhibits superior robustness compared with the traditional capacitor current active damping control.

KEYWORDS

active damping, robustness, LCL resonance, stability, coprime factorization

1 Introduction

Grid-connected inverters serve as critical interfaces between distributed energy resources and the power grid, playing an essential role in enhancing system efficiency, power quality, and reliability (Jinming et al., 2016). To meet grid connection standards, the output current of inverters must be filtered to reduce total harmonic distortion (THD). Typically, grid-connected inverter filters include L and LCL types. While the L filter is simple in design, its high-frequency harmonic attenuation performance is weak. Achieving effective harmonic suppression with L filters necessitates either larger inductance values or higher switching frequencies (Sosa et al., 2014). In contrast, LCL filters offer superior high-frequency harmonic suppression, along with advantages in terms of reduced size and cost, thus garnering widespread application (Wu et al., 2023). Nevertheless, LCL filters are prone to resonance issues that can destabilize grid-side current control (Chen et al., 2022). Researchers have proposed multiple solutions to mitigate the resonance problems associated with direct grid-side current control.

The traditional capacitor current active damping (CCAD) approach is widely used due to its simple implementation. The inner loop of the capacitor current is used to achieve active damping to suppress LCL resonance, and the outer loop of the grid-connected current directly controls the grid current through the proportional-integral (PI) controller (Zhi-ying et al., 2009; He et al., 2019; Pan et al., 2013). However, the large ripple in the filter capacitor current weakens the active damping (AD) effect. Additional current sensors are required, increasing the control cost (NIU et al., 2023; Xin et al., 2017). Chen et al. (2022) proposed a design method for optimal damping ratio based on CCAD. However, the impact of sampling and computational time delays on the AD ratio is not compensated. Wang et al. (2023) proposed a method of AD implementation based on capacitor voltage differential feedback. This method replaces the capacitor current with the differential of the capacitor voltage, which can suppress LCL resonance without the need for extra current sensors, thus reducing system cost. However, the differential operation will amplify measure noise, which reduces the damping effect and in turn, affects the grid-connect current quality. Ma et al. (2021) and Zhao et al. (2022) proposed full-dimensional/reduced-dimensional state observers to estimate the capacitor current, but this estimation method relies on an accurate system model and can also affect the dynamic behavior of the system. Dragievic et al. (2019) proposed a predictive current control model that has the advantages of good dynamic performance and easy implementation, but this algorithm relies on accurate parameters of the grid-side equivalent inductance. In the case of grid-side inductance perturbation, an indirect grid-side current control method is proposed by Marcos et al. (2018) and Zhou and Lu (2002), which indirectly controls the grid-connected current by controlling the inverter-side current. This method avoids the resonance problem brought by direct control of the grid-connected current. However, resonance may occur between the grid-side inductance and the filter capacitor due to a perturbation in the grid-side inductance, leading to distortion in the grid-connected current.

In summary, parametric uncertainties due to the aging of LCL filter components, magnetic core saturation, or perturbations in grid-side inductance can degrade the performance of AD that is designed based on the above classical control theory, resulting in inadequate robustness.

H∞ control offers advantages for models with parameter uncertainty. Recently, the H∞ robust control method has been applied to implement AD. A standard H∞ mixed sensitivity robust control method is proposed to regulate the output voltage of the nominal system under input voltage fluctuations cases (Wu et al., 2021). Gholami-Khesht (2021) designed the H∞ controller assigned to integrators from an optimal solution of a convex optimization problem subject to some LMI conditions. Chen and Ye (2024) explored the influence of AD filters on the LCL filter's resonant peak and proposed a robust H∞ AD filter with a preserved resonant peak. However, the above AD filters based on the H∞ control method were implemented by sensitivity weighting functions, input weighting functions, and output weighting functions. The selection of weighting functions can be troublesome and requires repeated attempts.

The H∞ control method focuses on minimizing the transfer function from external inputs to evaluation signals under the worst disturbance. The AD is obtained during the process. The AD design lacks intuitiveness and relies on design experience. Unlike traditional H∞ control, the design process of H∞ loop-shaping control is straightforward and simplified. It has the following characteristics: (1) the algorithm implementation is simple, and no iteration is required. (2) The robust stability margin can be calculated precisely. (3) The H∞ norm is not a performance index but rather a stability margin. H∞ loop-shaping control is used in the control of train systems, spacecraft, and nonlinear hard disk drive (HDD) systems (Cheng et al., 2024; Faure et al., 2022; Shaikh et al., 2024). Few studies have researched the application of H∞ loop-shaping control methods for LCL-type grid-connected inverters. It deserves further research.

To enhance the robustness of AD for grid-connected current control and simplify the complexity of control design, this article proposes a novel robust active damping (RAD) control method based on H∞ loop shaping, which does not require an additional current or voltage feedback loop. It shapes the high-, medium-, and low-frequency characteristics of the open-loop transfer function's magnitude–frequency curve directly by choosing appropriate weight functions to satisfy specific performance objectives (Liu et al., 2021). This concept of loop shaping is consistent with classical control principles, where control performance is achieved through weight functions. Additionally, robustness is guaranteed by applying the small-gain theorem. The H∞ loop-shaping controller combines weight functions and H∞ control, thus integrating the advantages of both classical loop shaping and H∞ control techniques.

The remainder of this article is organized as follows: Section 2 provides an overview of the modeling and design of an AD controller based on H∞ loop shaping. In Section 3, the RAD realization method is presented. In Section 4, a robustness analysis and comparison is conducted between the RAD and CCAD. In Section 5, an experimental comparative analysis is presented between the CCAD and RAD control strategies. Finally, conclusions are drawn in Section 6.

2 Modeling and design of an AD controller based on H∞ loop shaping

2.1 The mathematical model of the grid-connected inverter

A typical LCL-type inverter grid-connected topology is shown in Figure 1. It consists of a three-phase bridge inverter, an inverter-side inductor L_1, a filter capacitor C, a grid-side inductor L_2, and a grid inductor L_g. U_{dc} is the DC bus voltage, and C_{dc} is the DC bus capacitor. The grid-connected current control block diagram shown in Figure 2 is based on the circuit topology shown in Figure 1.

According to Figure 2, the transfer function from inverter voltage to grid-connected current is as follows:

$$G_{iL2} = \frac{i_{L2}(s)}{u_{inv}(s)} = \frac{1}{L_1 L_{2eq} C} \frac{1}{s\left(s^2 + \omega_r^2\right)}. \tag{1}$$

ω_r is the resonant frequency of the LCL inverter, which can be expressed as:

$$\omega_r = \sqrt{\frac{L_1 + L_{2eq,}}{L_1 L_{2eq} C}}$$

where $L_{2eq} = L_2 + L_g$.

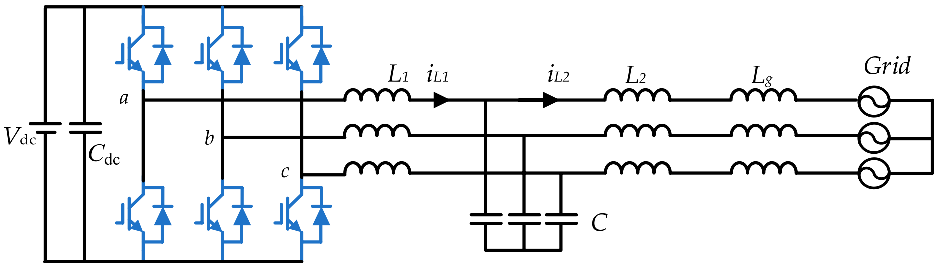

FIGURE 1
Topology of the LCL-type grid-connected VSI.

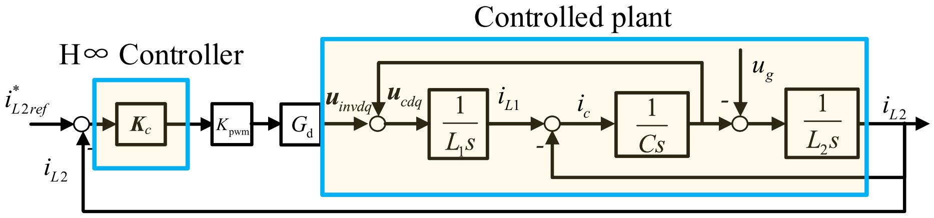

FIGURE 2
Control block diagrams of the LCL-type grid-connected VSI.

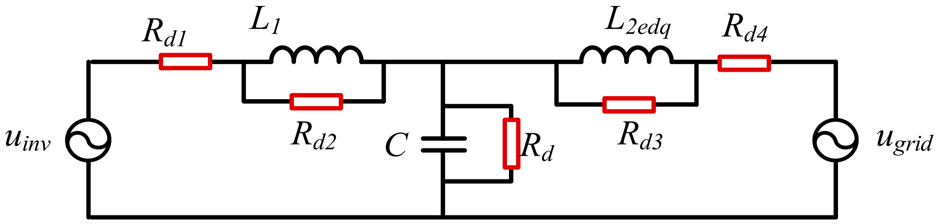

FIGURE 3
Various implementation methods of PD for the LCL-type grid-connected VSI.

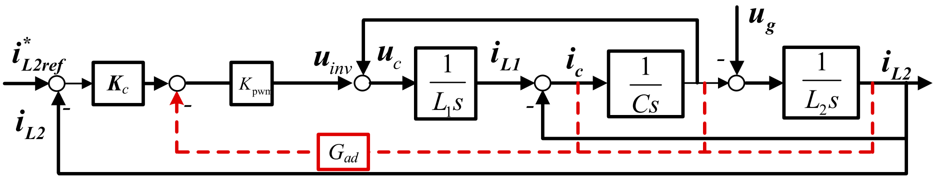

FIGURE 4
Active damping control block diagram with capacitor current feedback, capacitor voltage feedback, and grid-side current feedback.

The computation and pulse width modulated (PWM) delay can be approximated to one and a half of the sampling periods. Consequently, the total time delay can be expressed as

$$G_d = e^{-1.5T_s s} = \frac{1}{1 + 1.5T_s s}.$$

2.2 Active damping design

As illustrated in Figure 3, passive damping (PD) can be realized through various configurations of resistors, including series resistors with grid-side inductance, parallel resistors with grid-side

TABLE 1 Active damping and passive damping grid-connected current transfer function.

AD method	AD controller gad	AD method transfer function	PD method transfer function
Capacitor current feedback	K_{ad}	$\frac{1}{L_1 L_{2eq} C s^3 + K_{PWM} G_{ad} L_{2eq} C s^2 + (L_1 + L_{2eq}) s}$	$\frac{1}{L_1 L_{2eq} C s^3 + \frac{L_1 L_{2eq}}{R_d} s^2 + (L_1 + L_{2eq}) s}$
Capacitor voltage feedback	$K_{ad} s$	$\frac{1}{L_1 L_{2eq} C s^3 + K_{PWM} G_{ad} L_{2eq} s + (L_1 + L_{2eq}) s}$	
Grid current feedback	$K_{ad} s^2$	$\frac{1}{L_1 L_{2eq} C s^3 + K_{PWM} G_{ad} + (L_1 + L_{2eq}) s}$	

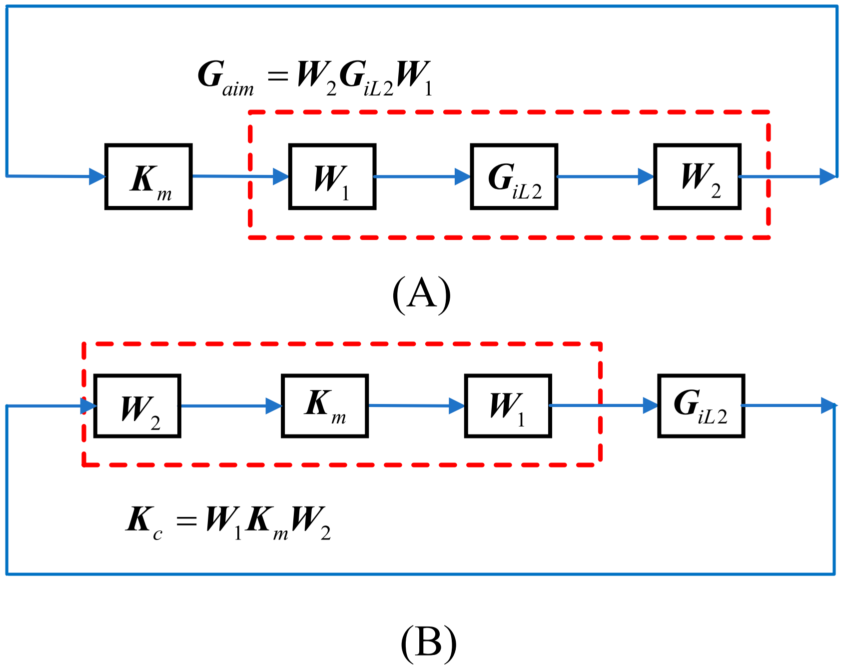

FIGURE 5
Implementation process of the H∞ loop-shaping method: **(A)** Construction of the desired transfer function and **(B)** formation of the H∞ loop-shaping controller.

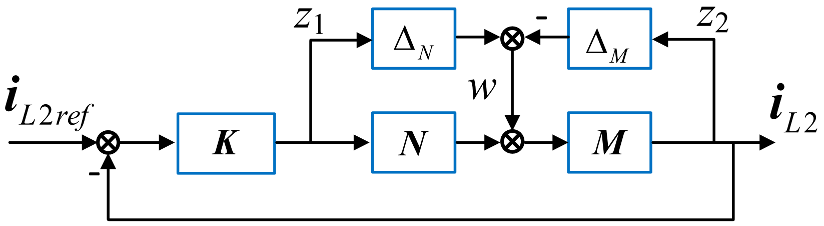

FIGURE 6
The feedback control block diagram in the form of coprime factorization.

inductance, series resistors with capacitor branch, parallel resistors with capacitor branch, series resistors with inverter-side inductance, and parallel resistors with inverter-side inductance. Among these configurations, the PD achieved by paralleling a resistor with a capacitor is particularly effective in suppressing resonance peaks in the mid-frequency band while maintaining the original frequency characteristics in both low- and high-frequency bands. Utilizing this PD approach, the G_{iL2} and the equivalent damping ratio can be expressed as follows:

$$G_{iL2}(s) = \frac{1}{L_1 L_{2eq} C} \frac{1}{s(s^2 + 2\xi\omega_r s + \omega_r^2).} \tag{2a}$$

$$\zeta = \frac{1}{2\omega_r R_d C.} \tag{2b}$$

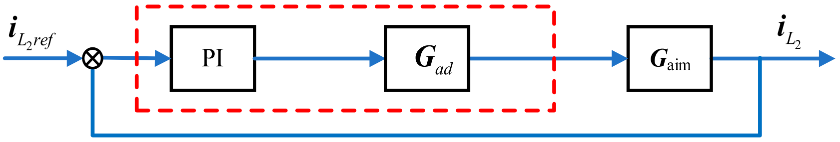

FIGURE 7
Equivalent block diagram of RAD.

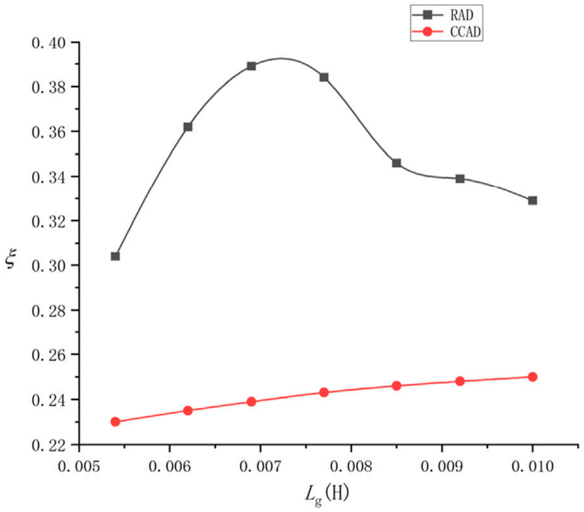

FIGURE 8
Curve of ξ with respect to L_{2eq}.

TABLE 2 Grid-connected inverter system parameters.

Parameter	Value	Parameter	Value
Grid voltage u_s/V	110	Grid-side inductor L_2/mH	1.2e-3
DC-side voltage u_{dc}/V	322	Grid impedance L_g/mH	6.5e-3
Inverter-side inductor L_1/mH	2.5e-3	Switch frequency f_{sw}/kHz	10
Filter capacitor C/μF	2.2e-6	Sample frequency f_s/kHz	10
Inverter gain K_{pwm}	1		

The control block diagram for AD with capacitor current, capacitor voltage, and grid-side current feedback is illustrated in Figure 4. The G_{iL2} with the above AD control is summarized in Table 1 (Chen et al., 2023). Here, K_{ad} represents the proportional controller coefficient, and G_{ad} denotes the feedback controller. When active damping is achieved using the capacitor current, G_{ad} serves as a proportional controller. When it is achieved using the capacitor voltage, G_{ad} serves as a first-order derivative controller, and when it is achieved using the grid current, G_{ad} serves as a second-order derivative controller.

From Table 1, it is evident that the structure of G_{iL2} with various AD controllers is the same as the PD control with the capacitor parallel resistors. Although the aforementioned AD method is equivalent to the capacitive parallel resistive damping (CPRD) method, it requires additional sensors. The H∞ loop-shaping method is used to reshape the open-loop transfer function of the LCL filter-based inverter without additional sensors. The reshaped open-loop transfer function is the same as that of the CPRD. Therefore, the RAD has the same damping performance as the CPRD.

H∞ loop-shaping control is composed of the weight function and the controlled plant. The high cutoff frequency is set in the mid-frequency range, the high gain is set in the low-frequency range, and the low gain is set in the high-frequency range. This gives the closed-loop system good dynamic and static characteristics. The original controlled plant G_{iL2} exhibits resonant peaks in the high-frequency range, which must be eliminated by the weighting function so as to realize the function of the AD. A PI weight function is applied to G_{iL2} to improve control dynamics.

The implementation process of the H∞ loop-shaping method is shown in Figure 5A. The plant G_{iL2} shown in Equation 1 is shaped into the desired transfer function G_{aim} using a pre-weighting function W_1 and a postweighting function W_2. Then, the normalized coprime factorization of G_{aim} is performed. According to the small-gain theorem, the intermediate controller K_m with the advantage of robustness can be obtained. Finally, K_m along with W_1 and W_2 forms the final H∞ loop-shaping controller K_c, as shown in Figure 5B. Control performance is achieved through weight functions, and robust stability is achieved by K_m. Thus, K_c integrates the advantages of both classical loop shaping and H∞ control techniques.

Based on the implementation process of the H∞ loop-shaping method, this article proposes the following RAD implementation method:

A damping term ξ is embedded to form the desired transfer function:

$$G_{aim} = \frac{1}{L_1 L_2 C} \frac{1}{s\left(s^2 + 2\xi\omega_0 s + \omega_0^2\right)}. \tag{3}$$

From Equation 3, it can be seen that the structure of the desired transfer function is the same as Equation 2, which ensures the proposed RAD has the same damping function as the PD method. The weighting transfer function to achieve the desired transfer function can be derived as

$$\begin{cases} W_1 = \dfrac{G_{aim}(S)}{G_{iL2}(S)} = \dfrac{s^2 + \omega_0^2}{s^2 + 2\xi\omega_0 s + \omega_0^2}. \\ W_2 = 1 \end{cases} \tag{4}$$

The selection of the aforementioned weighting function is determined based on the desired transfer function, thereby

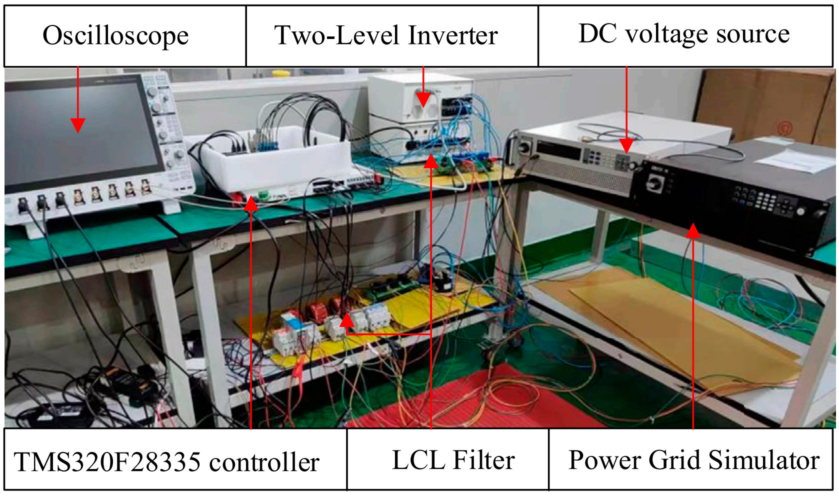

FIGURE 9
Three-phase LCL grid-connected inverter experimental platform.

TABLE 3 CCAD control parameters.

Parameter category	Value
Capacitive current proportional coefficient	55
Integral coefficient	68.112
Proportional coefficient	7.4923e+03

reducing the number of trial-and-error cycles required to select the weighting function. Because G_{iL2}, W_1 and W_2 are all scalar transfer functions, W_1GW_2 is equivalent to W_1W_2G. W_1W_2 can be treated as a single transfer function for the overall design, which is equivalent to setting W_2 to 1 and only designing W_1, thereby simplifying the design process.

Furthermore, as shown in Figure 5B, the H∞ loop-shaping controller described by Equation 5 is composed of W_1, W_2, and K_m. This allows the required damping for the undamped controlled plant (1) to be achieved through K_c.

$$K_c = W_2 K_{\boldsymbol{m}} W_{\boldsymbol{1}} = \frac{s^2+\omega_0^2}{s^2+2\xi\omega_0 s+\omega_0^2} K_m. \tag{5}$$

2.3 Design for improved dynamic and steady-state performance

To ensure the system's steady-state accuracy and response speed, a PI controller is applied to the damped controlled plant whose transfer function is shown in (5). Then G_{aim} can be derived as (8). This allows the mid-frequency bandwidth of the target transfer function to be flexibly adjustable via the PI controller, which also increases steady-state accuracy, thereby simultaneously enhancing both steady-state performance and dynamic tracking performance.

$$G_{aim}(s) = \frac{1}{L_1L_2C}\frac{1}{s\left(s^2+2\xi\omega_0 s+\omega_0^2\right)}\left(K_p+\frac{K_i}{s}\right), \tag{6}$$

where K_{p} is the proportional controller coefficient, and K_{i} is the integral controller coefficient.

G_d will change the position of the resonance points, thereby reducing the damping effect. To offset the impact of G_d, a composite derivative $1/G_d$ is applied to Equation 8. Then, the G_{aim} can be expressed as

$$G_{aim}(s) = \frac{1}{L_1L_2C}\frac{1}{s\left(s^2+2\xi\omega_0 s+\omega_0^2\right)}\left(K_p+\frac{K_i}{s}\right)\frac{1}{G_d}.$$

Correspondingly, Equation 6 and K_c are revised as (10) and (11), respectively.

$$\begin{cases} W_1 = \dfrac{s^2+\omega_0^2}{s^2+2\xi\omega_0 s+\omega_0^2}\left(K_p+\dfrac{K_i}{s}\right)\dfrac{1}{G_d.} \\ W_2 = 1 \end{cases} \tag{7}$$

$$K_c = \frac{s^2+\omega_0^2}{s^2+2\xi\omega_0 s+\omega_0^2}\left(K_p+\frac{K_i}{s}\right)\frac{1}{G_d}K_m. \tag{8}$$

3 The solution to the H∞ loop-shaping controller

First, a normalized coprime factorization of the perturbed plant model $G_{\Delta m}$ is carried out. Subsequently, the robust stability criterion is used to derive K_m. Finally, the K_c is deduced by multiplying K_m with both W_1 and W_2.

3.1 Coprime factorization

The normalized left coprime factorization of G_{aim} is

$$G_{aim} = M^{-1}N. \tag{9}$$

Here, M and N are stable coprime transfer functions that satisfy the equation $MM^T + NN^T = 1$.

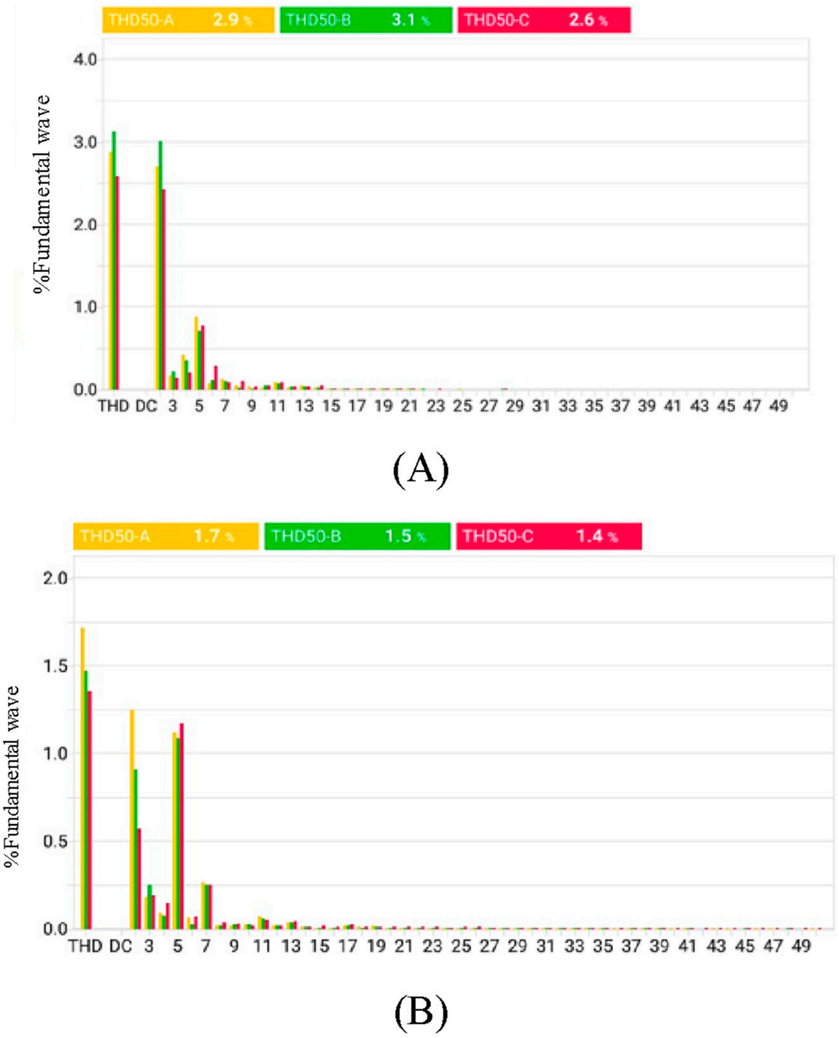

FIGURE 10
Harmonics of grid-side current under steady-state conditions. **(A)** CCAD control strategy and **(B)** RAD control strategy.

Based on Equation 9, the left coprime factorization of G_{aim} with perturbation is

$$G_{\Delta m} = (M + \Delta_M)^{-1}(N + \Delta_N). \tag{10}$$

Here, Δ_M and Δ_N are the uncertainty in G_{aim}.

The standard feedback control system in the form of coprime factorization is shown in Figure 6 based on Equation 10.

3.2 Deriving the solution for the controller

For the perturbed feedback system of Figure 6, the system stability is robust according to the small-gain theorem, which requires Equation 11 to be satisfied.

$$\left\| \begin{bmatrix} K_m \\ 1 \end{bmatrix} (1 + G_{aim}K_m)^{-1} M^{-1} \right\|_\infty \le \lambda = \varepsilon^{-1,} \tag{11}$$

where λ is the H∞ norm from w to $\begin{bmatrix} i_{L2} \\ i_{L2ref} - i_{L2} \end{bmatrix}$, and generally, the value of λ is required to be no greater than 4–5 (Sigurd, 2005; Lanzon and Tsiotras, 2005; He et al., 2010). ε represents the stability margin of the response.

Because the norms of the normalized coprime factorizations M and N are both less than 1, (14) can be transformed into Equation 12 without coprime factors, thereby simplifying the controller design.

$$\left\| \begin{bmatrix} K_m \\ 1 \end{bmatrix} (1 + G_{aim}K_m)^{-1} \begin{bmatrix} 1 & G_{aim} \end{bmatrix} \right\|_\infty \le \lambda = 1 \big/ \varepsilon \tag{12}$$

The minimum value of λ must be calculated to ensure the robustness of the controller. The value can be calculated as

$$\lambda_{\boldsymbol{min}} = \left\{1 - \left\| \begin{bmatrix} N & M \end{bmatrix} \right\|_H^2 \right\}^{-1/2} = \left(1 + \rho(\boldsymbol{XZ})\right)^{1/2,} \tag{13}$$

where $\|.\|_H$ denotes the Hankel norm, ρ denotes the spectral radius, and $\boldsymbol{X}$ and $\boldsymbol{Z}$ are the solutions of the algebraic Riccati Equation 14.

$$\begin{cases} \boldsymbol{AZ} + \boldsymbol{ZA}^T - \boldsymbol{ZC}^T\boldsymbol{CZ} + \boldsymbol{BB}^T = 0 \\ \boldsymbol{A}^T\boldsymbol{X} + \boldsymbol{XA} - \boldsymbol{XBB}^T\boldsymbol{X} + \boldsymbol{C}^T\boldsymbol{C} = 0, \end{cases} \tag{14}$$

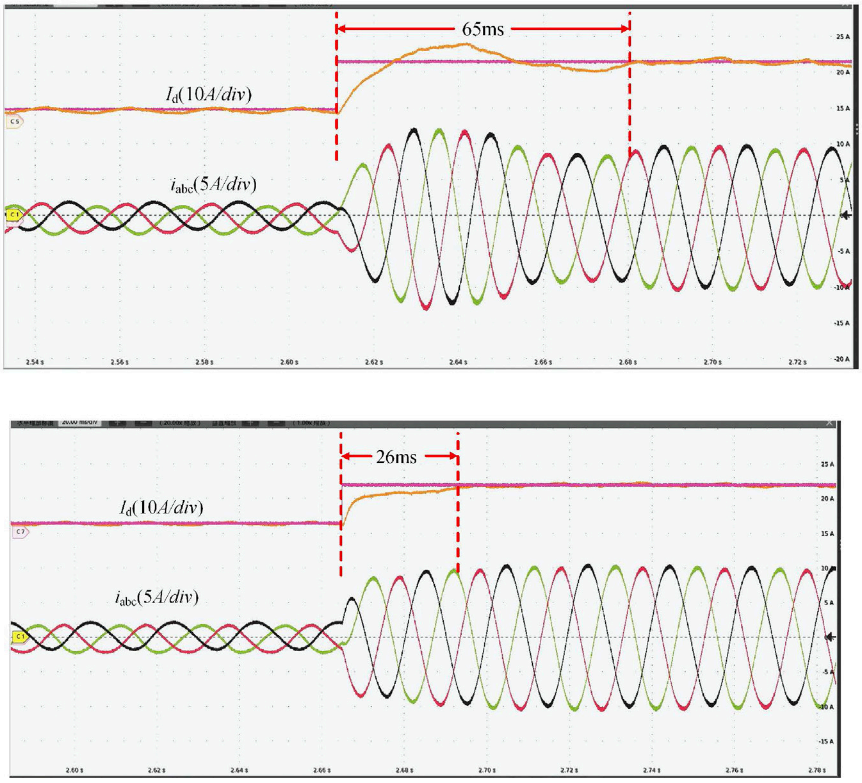

FIGURE 11
Waveforms of active current and grid-side three-phase current when the active reference current suddenly changes. **(A)** CCAD control strategy and **(B)** RAD control strategy.

where $(\boldsymbol{A}, \boldsymbol{B}, \boldsymbol{C}, \boldsymbol{D})$ is the minimal state-space realization of $G_{\boldsymbol{aim}}$.

For the specified $\lambda > \lambda_{\min}$, the K_m that satisfies in Equation 11 is as follows:

$$K_m = \boldsymbol{B}^T \boldsymbol{X}\left[s\boldsymbol{I} - \boldsymbol{A} - \boldsymbol{BF} - \gamma^2 \left(\boldsymbol{L}^T\right)^{-1} \boldsymbol{ZC}^T \boldsymbol{C}\right]^{-1} \gamma^2 \left(\boldsymbol{L}^T\right)^{-1} \boldsymbol{ZC}^T, \quad (15)$$

where $\boldsymbol{F} = -B^T\boldsymbol{X}$, $\boldsymbol{L} = (1-\gamma^2)\boldsymbol{I} + \boldsymbol{XZ}$. K_m, W_1, and W_2 constitute the final loop-shaping controller K_c, as shown in Equation 8.

From Equation 12, it can be seen that, unlike the classical PI controller, the H∞ loop-shaping controller does not have a specific structure. Its design depends on the shape of the objective function and the stability margin considering system uncertainties, thus offering greater design flexibility.

4 Robustness comparative analysis

Based on Equation 11, it is evident that the designed K_c in this study comprises three segments: PI, G_{ad}. Consequently, the system control block diagram can be revised, as illustrated in Figure 7. Where $G_{ad} = \frac{s^2+\omega_0^2}{s^2+2\xi\omega_0 s+\omega_0^2}\frac{1}{G_d}K_m$, G_{ad} contributes AD to the system and, at the same time, offsets system delay G_d, the PI controller ensures dynamic and static performance of the closed-loop system. ξ can be obtained with the RAD control method as shown by the black curve in Figure 8.

Using the experimental parameters shown in Table 2, the damping ratio ξ can be obtained according to Chen et al. (2023) with the CCAD control method when the values of L_{2eq} vary within ±30% range, as shown by the red curve in Figure 8. ξ can also be obtained with the RAD control method as shown by the black curve in Figure 8.

As shown in Figure 8, when the values of L_{2eq} vary within the ±30% range, the ξ of the RAD control is always greater than that of the CCAD control. The robustness of the RAD control is superior. This is because there is a delay compensation term $1/G_d$ in controller K_c, which offsets the impact of system delay. Therefore, it exhibits better robustness than the CCAD control.

5 Experimental verification

An experimental platform was set up to verify the effectiveness of the RAD control method proposed in this article, as shown in Figure 9. The performance of the RAD was compared with that of the CCAD. The steady-state performance, dynamic response, and robustness to inductance change were evaluated. The RTU-BOX201 controllers and the RTI-INV6020IR inverters were both produced by Nanjing Ruitu Youte Technology Co., Ltd., and the grid simulator was the Chroma 61815. The circuit parameters of the experimental system are listed in Table 2.

For the desired transfer function in Equation 7, with ξ set to the optimal damping ratio of 0.707 and taking into account both the system's response speed and steady-state error, K_p is set to 65, and K_i is set to 188, respectively. Based on the circuit

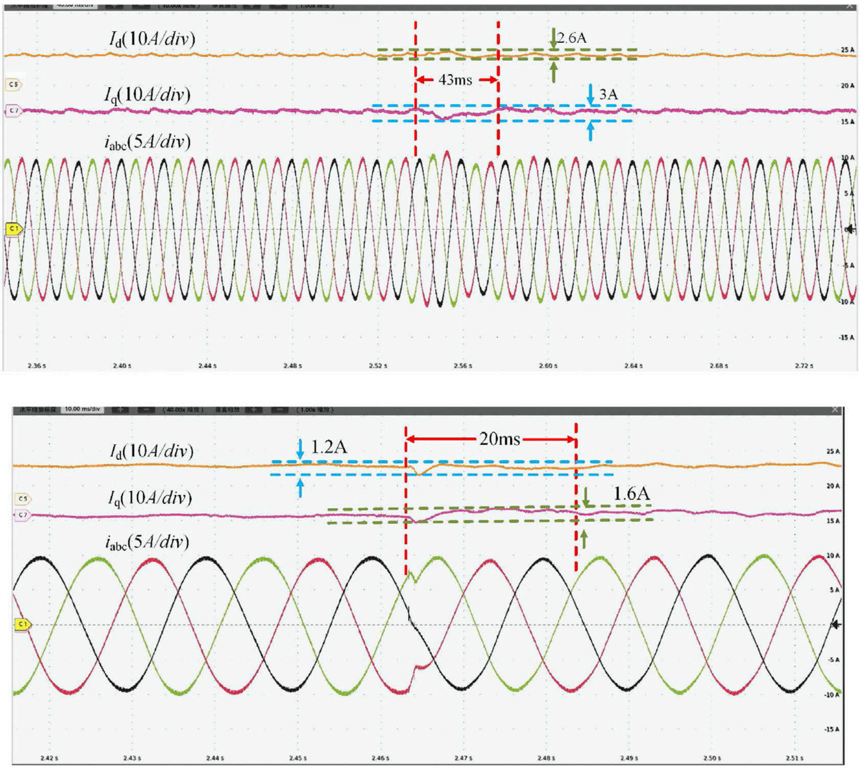

FIGURE 12
Experimental waveform of the grid-side current i_{abc} when L_{2eq} suddenly increases by 30%: **(A)** CCAD control strategy and **(B)** RAD control strategy.

parameters shown in Table 2, K_c can be obtained from Equations 11, 14, 15:

$$K_c = \frac{-43.54s^4 + 1.748 \times 10^7 s^3 - 2.062 \times 10^{11} s^2 + 2.749 \times 10^{15} s + 5.577 \times 10^{17}}{s^4 + 2.793 \times 10^5 s^3 + 7.843 \times 10^9 s^2 + 1.432 \times 10^{14} s}.$$

$\lambda_{\min}$ is usually required to be less than 4, corresponding to a 25% allowed coprime uncertainty (Sigurd, 2005). From Equation 13, it can be deduced that $\lambda_{\min}$ is 3, which is less than commonly required value and ensures the robustness of system.

CCAD control parameter design: according to the CCAD control method proposed by Chen et al. (2023), K_{ad} is set to 55. The bandwidth of the current loop is generally taken as 1/10 of the switching frequency, and the phase margin is set to 45° (Yang et al., 2021). The control parameters listed in Table 3 are obtained.

5.1 Steady-state performance analysis

The harmonic levels of grid current for the CCAD and RAD control strategies are illustrated in Figure 10. As depicted in Figure 10A, the total harmonic distortion (THD) of the three-phase grid-side current under the CCAD control strategy is 3.1%. Figure 10B shows that the THD of the three-phase grid-side current with the RAD control strategy is 1.7%. The experimental results demonstrate that the RAD control strategy yields a lower THD in the grid-side current. This improvement is attributed to the higher damping ratio of the proposed method.

5.2 Dynamic characteristic analysis

The dynamic response of the CCAD control strategy is shown in Figure 11A. When the reference active current i_{dref} steps from 2 A to 10 A, the measured active current i_d follows the command with a large overshoot. The regulation time is 65 m. Figure 11B is the experimental waveforms of the grid-connected current with the RAD control strategy under the same command. The regulation time is 26 m with little overshoot. The experimental results show that the dynamic response of the proposed RAD control strategy is superior to that of the CCAD control strategy. This is because the RAD control method exhibits a higher damping ratio than the CCAD method, significantly shortening the system's transient transition time. This result indicates that the RAD control strategy has a significant advantage in improving the system's dynamic response.

5.3 Robustness analysis under the perturbation of grid-side inductance parameters

Figure 12 shows the waveforms of active current i_d, reactive current i_q, and grid-side three-phase current i_{abc} when the grid-side inductance suddenly increases by 30%. Under CCAD control, the maximum i_d fluctuation is 2.6 A, the maximum i_q fluctuation is 3 A, and the regulation time is 43 m. Under RAD control, the maximum i_d fluctuation is 1.2 A, the maximum i_q fluctuation is 1.6 A, and the

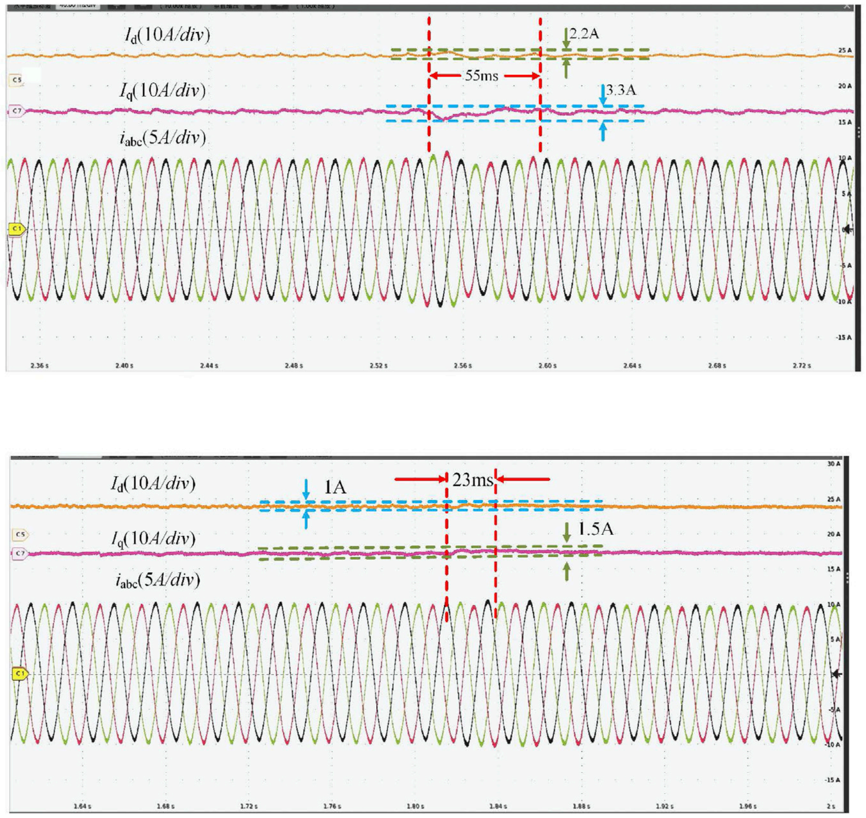

FIGURE 13
Experimental waveform of the grid-side current i_{abc} when L_{2eq} suddenly decreases by 30%: **(A)** CCAD control strategy and **(B)** RAD control strategy.

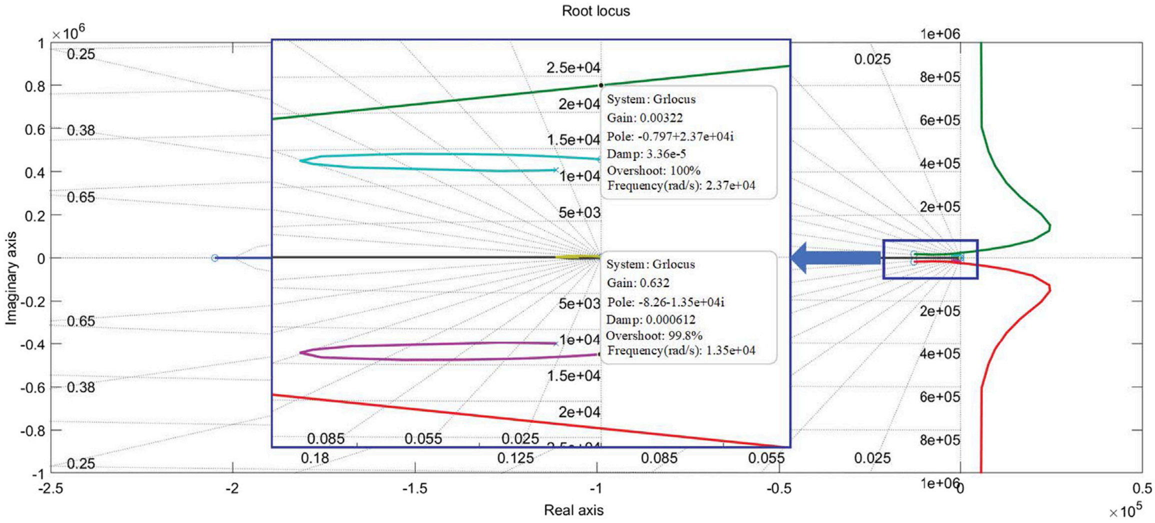

FIGURE 14
The root locus of the system when L_g varies.

regulation time is 20 m. The RAD control strategy results in shorter current regulation time and better robustness.

Figure 13 shows the waveforms of the active current i_d, the reactive current i_q, and the grid-side three-phase current i_{abc} when the grid-side inductance suddenly decreases by 30%. Under CCAD control, the maximum i_d fluctuation is 2.2 A, the maximum i_q fluctuation is 3.3 A, and the regulation time is 55 m. Under RAD control, the maximum i_d is 1 A, the maximum

TABLE 4 The total harmonic distortion (THD) of the grid-side current under grid-side inductance perturbation.

Control strategy	Total harmonic distortion (THD) %		
	When the steady-state condition inductance increases by 30%, the inductance decreases by 30%		
CCAD	3.1	4.6	5.1
RAD	1.7	2.7	2.4

i_q fluctuation is 1.5 A, and the regulation time is 23 m. RAD control strategy results in shorter current regulation time and better robustness.

Due to the constraints of experimental conditions, the root locus method is used to determine the allowable range of variation for L_g. The range of variation for L_g is from 0.003 to 0.5, as shown in Figure 14.

Table 4 lists the THD of the grid-side current with RAD and CCAD. The data presented in Table 4 indicate that the grid-side current THD with the RAD control strategy consistently remains lower than that with the CCAD control strategy.

Under the aforementioned operating conditions, the RAD control strategy exhibits superior robustness and lower THD. This enhanced performance is attributed to the higher damping ratio achieved by the proposed control method compared to the CCAD approach under varying grid-side inductance conditions. The robustness and disturbance rejection capabilities of the proposed method enable the system to maintain more stable performance amid external disturbances induced by grid-side inductance variation.

6 Conclusion

This study presents a novel RAD control strategy based on H∞ loop-shaping technology to address the robustness insufficiency of the conventional AD control methods. This control strategy avoids introducing a new feedback control loop with additional sensors or state observers via H∞ loop-shaping technology, reducing costs and enhancing robustness. Through extensive analysis and experimental comparison, it is found that the RAD control exhibits a high active damping ratio compared with that of the CCAD under various grid-side inductances, demonstrating better dynamic and static performance.

Data availability statement

The original contributions presented in the study are included in the article/Supplementary Material; further inquiries can be directed to the corresponding author.

Author contributions

WS: formal analysis, investigation, methodology, software, and writing–original draft. WG: methodology and writing–review and editing. GX: conceptualization, data curation, and writing–review and editing. TW: conceptualization, data curation, and writing–review and editing. CS: validation and writing–review and editing. ZL: resources and writing–review and editing. HX: resources and writing–review and editing. ZH: data curation and writing–review and editing. JL: resources and writing–review and editing. JS: resources and writing–review and editing. RM: writing–review and editing. SS: writing–review and editing. XL: writing–review and editing. YH: writing–review and editing.

Funding

The author(s) declare that financial support was received for the research, authorship, and/or publication of this article. This work was supported by the Fundamental Research Funds for the Central Universities (Grant No. 2022XKRC018) and the National Key R&D Program of China (Grant Nos. 2022YFB2402900 and 52060023001T).

Conflict of interest

Authors ZL and HX were employed by the State Grid Shandong Electric Power Company. Author JL was employed by the R&D Department at Hiconics Eco-energy Technology Co.

The remaining authors declare that the research was conducted in the absence of any commercial or financial relationships that could be construed as a potential conflict of interest.

Publisher's note

References

Chen, S., and Ye, Y. (2024). Robust H∞ active damping filter with preserved resonant peak for resonant harmonic suppression. *IEEE J. Emerg. Sel. Top. POWER Electron.* 12 (3), 2580–2591. doi:10.1109/JESTPE.2024.3375302

Chen, W., Zhang, Y., Tu, Y., Guan, Y., Shen, K., and Liu, J. (2023). Unified active damping strategy based on generalized virtual impedance in LCL-type grid-connected inverter. *IEEE Trans. Industrial Electron.* 70 (8), 8129–8139. doi:10.1109/TIE.2022.3232647

Chen, W., Zhang, Y., Tu, Y., Shen, Ke, and Liu, J. (2022). Active damping control for LCL filters with inverter-side current feedback only. *IEEE Trans. Power Electron.* 37 (9), 10065–10069. doi:10.1109/TPEL.2022.3159229

Cheng, S., Ma, L., Liu, F., Ge, X., and Zhou, K. (2024). Low-frequency oscillation suppression of train–grid coupling systems by H∞ loop shaping. *IEEE Trans. Transp. Electrification* 10 (2), 4470–4483. doi:10.1109/TTE.2023.3314007

Dragievic, T., Zheng, C., Rodriguez, J., and Blaabjerg, F. (2019). Robust quasi-predictive control of LCL-Filtered grid converters. *IEEE Trans. Power Electron.* 35 (2), 1934–1946. doi:10.1109/TPEL.2019.2916604

Faure, M., Henry, D., and Cieslak, J. (2022). A H∞ control solution for space debris removal missions using robotic arms: the ESA e.Deorbit case. 2022 UKACC 13th International Conference on Control (CONTROL), Plymouth, United Kingdom. doi:10.1109/Control55989.2022.9781461

Gholami-Khesht, H. (2021). "Robust H∞ current control of three-phase grid connected voltage source converters using linear matrix inequalities," in *2021 IEEE 22nd workshop on control and modelling of power electronics*. Cartagena, Colombia. doi:10.1109/COMPEL52922.2021.9646071

He, Y., Wang, X., Ruan, X., Pan, D., Xu, X., and Liu, F. (2019). Capacitor-current proportional-integral positive feedback active damping for LCL-type grid-connected inverter to achieve high robustness against grid impedance variation. *IEEE Trans. Power Electron.* 34 (15), 12423–12436. doi:10.1109/TPEL.2019.2906217

He, Z., Fan-Wei, MENG, Liu, and Wang, G. (2010). Synthesis in H-infinity loop-shaping design. *ACTA AUTOM. SIN* 36 (6), 347–352. doi:10.3724/sp.j.1004.2010.00347

Jinming, X. U., Lin, J. I., Xiaowei, G. E., and Shaojun, X. I. E. (2016). LCL-Filter optimization design with consideration of inverter-side current feedback control impacts. *Proc. CSEE* 36 (17), 4656–4665. doi:10.13334/j.0258-8013.pcsee.151579

Lanzon, A., and Tsiotras, P. (2005). A combined application of H/sub/spl infin//loop shaping and/spl mu/-synthesis to control high-speed flywheels. *IEEE Trans. Control Syst. Technol.* 13 (5), 766–777. doi:10.1109/TCST.2005.847344

Liu, H., Lei, M. A., and Lin, PENG (2021). H∞ loop-shaping robust direct current control for single-phase PWM rectifier. *Power Syst. Technol.* 45 (4), 1429–1437. doi:10.13335/j.1000-3673.pst.2020.0637

Ma, A., Flora, L. D., and Husain, I. (2021). Observer based generalized active damping for voltage source converters with LCL filters. *IEEE Trans. Power Electron.* 37 (1), 125–136. doi:10.1109/TPEL.2021.3093504

Marcos, G. J., González, S. A., Fischer, J. R., Martinez, J. F., and Carrica, D. O. (2018). Inverter-side current control of grid-connected voltage source inverters with LCL filter based on generalized predictive control. *IEEE J. Emerg. Sel. Top. Power Electron.* 6 (4), 1732–1743. doi:10.1109/JESTPE.2018.2826365

Niu, C., Xiao, H., Li, M., Cao, Q., Yao, Z., Xiao, H., et al. (2023). Method of achieving active damping by filter capacitor voltage feedback with equivalent differential link. *Electr. Power Autom. Equip.* 43 (6), 204–210. doi:10.16081/j.epae.202211017

Pan, D., Ruan, X., Bao, C., Li, W., and Wang, X. (2013). Capacitor-currentfeedback active damping with reduced computation delay for improving robustness of LCL-type grid-connected inverter. *IEEE Trans. Power Electron.* 29 (7), 3414–3427. doi:10.1109/TPEL.2013.2279206

Shaikh, I., Matušů, R., Zerdazi, El W., and Wendimu, A. A. (2024). H∞ loop-shaping continuous-time controller design for nonlinear HDD systems: a reduced-order approach using hankel-norm approximation. *IEEE Access* 12, 111523–111534. doi:10.1109/access.2024.3441754

Sigurd, S. (2005). *Multivariable Feedback Control Analysis and design*. 2nd ed., 405–406. American: Hoboken.

Sosa, J. M., Escobar, G., Martínez-Rodríguez, P. R., Vazquez, G., and Diosdado, M. (2014). "Comparative evaluation of L and LCL filters in transformer less grid tied converters for active power injection," in *2014 IEEE international autumn meeting on power, electronics and computing (ROPEC), ixtapa, Mexico*, 1–6.

WANG, A., Ge, W., Li, T., Cui, D., Li, M., and Xiao, H. (2023). Research on realization technology of active damping method with differential feedback of filter capacitance voltage for LCL filter based grid-connected inverters. *J. Electr. Eng.* 18 (1), 126–132. doi:10.11985/2023.01.014

Wu, TSAI.-F. U., Chan, CHING.-CHIH, Chang, Y. U. N.-HSIANG, Chiu, J. Y., Hung, C. C., and Chuang, T. H. (2023). Grid-side current improvement with direct digital control and capacitor voltage feedforward to mitigate distorted grid currents for 3Φ3W LCL grid-connected inverter under distorted grid voltages. *IEEE Open J. Power Electron.* 5, 37–49. doi:10.1109/OJPEL.2023.3335220

Wu, X., Xu, C., Wei, B., Xia, C., and Li, X. (2021). H mixed sensitivity robust control method of relay ICPT system for output voltage regulation. *Electr. Eng.* 103, 781–792. doi:10.1007/s00202-020-01116-1

Xin, Z., Wang, X., Loh, P. C., and Blaabjerg, F. (2017). Grid-current-feedback control for LCL-filtered grid converters with enhanced stability. *IEEE Trans. Power Electron.* 32 (4), 3216–3228. doi:10.1109/TPEL.2016.2580543

Yang, L. I., Qi, R., and Ming-guang, D. A. I. (2021). Linear active disturbance rejection control with adjustable compensation factor applied for outer voltage control of inverter. *J. Zhejiang Univ. Eng. Sci.* 55 (7), 1279–1288. doi:10.3785/j.issn.1008-973X.2021.07.007

Zhao, J., Xie, C., Li, K., Zou, J., and Guerrero, J. M. (2022). Passivity-oriented design of LCL-type grid-connected inverters with luenberger observer-based active damping. *IEEE Trans. Power Electron.* 37 (3), 2625–2635. doi:10.1109/TPEL.2021.3109434

Zhi-ying, X. U., Ai-guo, X. U., and Shao-jun, X. I. E. (2019). Dual-loop grid current control technique for grid-connected inverter using an LCL filter. *Proc. CSEE* 29 (27), 36–41. doi:10.1109/MILCOM.2009.5379889

Zhou, X., and Lu, S. (2002). A novel inverter-side current control method of LCL -filtered inverters based on high-pass- filtered capacitor voltage feedforward. *IEEE Access* 8, 16528–16538. doi:10.1109/ACCESS.2020.2967122